Chemical Engineering Journal 444 (2022) 136631

Contents lists available at ScienceDirect

Chemical Engineering Journal

journal homepage: www.elsevier.com/locate/cej

Porous graphene foam composite-based dual-mode sensors for underwater temperature and subtle motion detection

Xue Chen [a], Runze Li [a], Guangyu Niu [b], Mingyang Xin [c], Guizhi Xu [a,*], Huanyu Cheng [d,*], Li Yang [c,*]

[a] State Key Laboratory of Reliability and Intelligence of Electrical Equipment, Key Laboratory of Bioelectromagnetics and Neuroengineering of Hebei Province, School of Electrical Engineering, Hebei University of Technology, Tianjin 300130, China
[b] Department of Architecture and Art, Hebei University of Technology, Tianjin 300130, China
[c] State Key Laboratory of Reliability and Intelligence of Electrical Equipment, School of Health Sciences and Biomedical Engineering, Hebei University of Technology, Tianjin 300130, China
[d] Department of Engineering Science and Mechanics, The Pennsylvania State University, University Park, PA 16802, United States

ARTICLE INFO

Keywords:
Laser-induced graphene foam composites
Dual-mode sensors
Waterproof and all-weather conditions
Subtle motion detections

ABSTRACT

Soft multimodal sensors in practical applications for health monitoring and human–machine interfaces require them to show sufficiently high sensitivity over wide sensing rages, rapid response and excellent durability, and waterproof property. Herein, we demonstrate a dual-mode sensor based on a porous graphene foam composite to achieve the aforementioned challenging yet attractive performance parameters for strain and temperature sensing. The resulting dual-mode sensor exhibits a strain sensitivity of 2212.5 in the wide piecewise linear range of 0–65%, a rapid response of 0.11 s, an ultralow detection limit of 0.0167%, and outstanding stability over 15,000 cycles. The sensor can also detect temperature with a high sensitivity of 0.97 $\times$ 10^{-2} °C $^{-1}$ over a wide linear range of 10–185 °C and a small detection limit for sensing both low- and high-temperature environments. Taken together with the waterproof property, the dual-mode sensor can accurately monitor the large, small, and even subtle motions and temperature variations in both dry and underwater conditions. The capability to detect the subtle yet rapidly changing motions from distal arteries and skeletal muscles paves the way for the development of future soft multimodal, waterproof electronic sensing devices toward human–computer interaction, health monitoring and early disease prevention, and personalized medicine.

1. Introduction

The rapid development of soft wearable sensing devices has advanced the forefronts for many emerging applications, including personal healthcare [1,2], electronic skin [3–5], human physiological signal monitoring [6–8], and human–machine interfaces [9–12]. However, the practical applications still call for high-performance soft multimodal sensors with waterproof performance to accurately detect various stimuli (e.g., strain, temperature, and pressure) in all-weather conditions (e.g., sweat or underwater). Inspired by the human skin, early efforts to detect strain or temperature focus on the exploration of composite materials with different conductivities or macro/micro structures [13–19]. Important examples include MoS_2-decorated laser-induced grapheme [20], crack-based designs [21], transparent sandwich structures with tunable permittivity and geometry [22].

Simultaneous detection of two stimuli such as temperature and strain with a dual-mode sensor can further simplify the setup and device complexity [23,24]. The simple idea is to combine strain-sensitive with thermosensitive materials, including laser-induced porous carbon on starch film [25], conductive nanopaper based on Ag nanowire/cellulose nanofiber [26], and mixed carbon black and reduced graphene oxide on paper [27]. However, these sensors exhibit a relatively narrow detection range or low sensitivity, which is not sufficient to accurately detect both large and small human motions or temperature. Efforts to increase the sensing range lead to the exploration of the strain- and temperature-responsive hydrogels with conductive nanomaterials [28–30]. The wide strain sensing range of greater than 300% comes at a cost of low sensitivity, presenting challenges to detect weak motion and temperature changes. The sensitivity could be slightly improved by using 2D-Bi_2S_3 embedded PVDF/PPy nanomembranes [31], but the expensive 2D-

* Corresponding authors.
E-mail addresses: gzxu@hebut.edu.cn (G. Xu), huanyu.cheng@psu.edu (H. Cheng), yangli5781@126.com (L. Yang).

https://doi.org/10.1016/j.cej.2022.136631
Received 27 February 2022; Received in revised form 7 April 2022; Accepted 25 April 2022
Available online 28 April 2022
1385-8947/

Bi_2S_3 and the complex preparation process make it even less attractive. In addition, the use of dual-mode sensors in high moisture or underwater conditions leads to the need for a separate superhydrophobic coating [32–34]. However, the dual-mode sensor with sufficiently high sensitivity over a wide sensing range, ultralow detection limit, rapid response and excellent durability, and waterproof property is yet to be reported.

Here, this work reports a high-performance, waterproof dual-mode sensor based on porous graphene foam composites prepared by a simple laser writing and transferring process. The dual-mode sensor exhibits a high strain sensitivity of 2212.5 and a broad working range for strain (0–65%) and temperature (10–185 ℃), ultralow detection limit (<0.0167%), and long-term reliability over 15,000 cycles. The resulting sensor could not only monitor large and small human movement and temperature variations in dry and underwater conditions, but also capture the subtle deformations such as pulse waveforms from distal arteries and subtle yet rapid skeletal muscle motions. The results presented in this work could be easily applied for movement disorder detection, rehabilitation, health monitoring in all-weather conditions, and future human–machine interactions.

2. Results and discussion

2.1. Fabrication of the Dual-Mode sensor

A facile and scalable laser direct writing process is exploited to create 3D porous graphene foams from carbon-containing materials such as the commercial polyimide thin films. Next, infiltration the pores with silicone elastomer followed by a transfer yields the dual-mode sensor (Figure S1). The detailed fabrication procedure of the dual-mode sensor is depicted in Experimental Section. The deformations of the sensor from the variations in the temperature or strain change the conductive pathway of the porous graphene foam and thus the resistance of the sensor (Figure S2). Besides functioning in dry conditions, the waterproof property of the sensor further allows the sensor to detect temperature and subtle motions/vibrations. The waterproof property of the sensor is conducted by the hydrophobic LIG/PDMS composite, while the

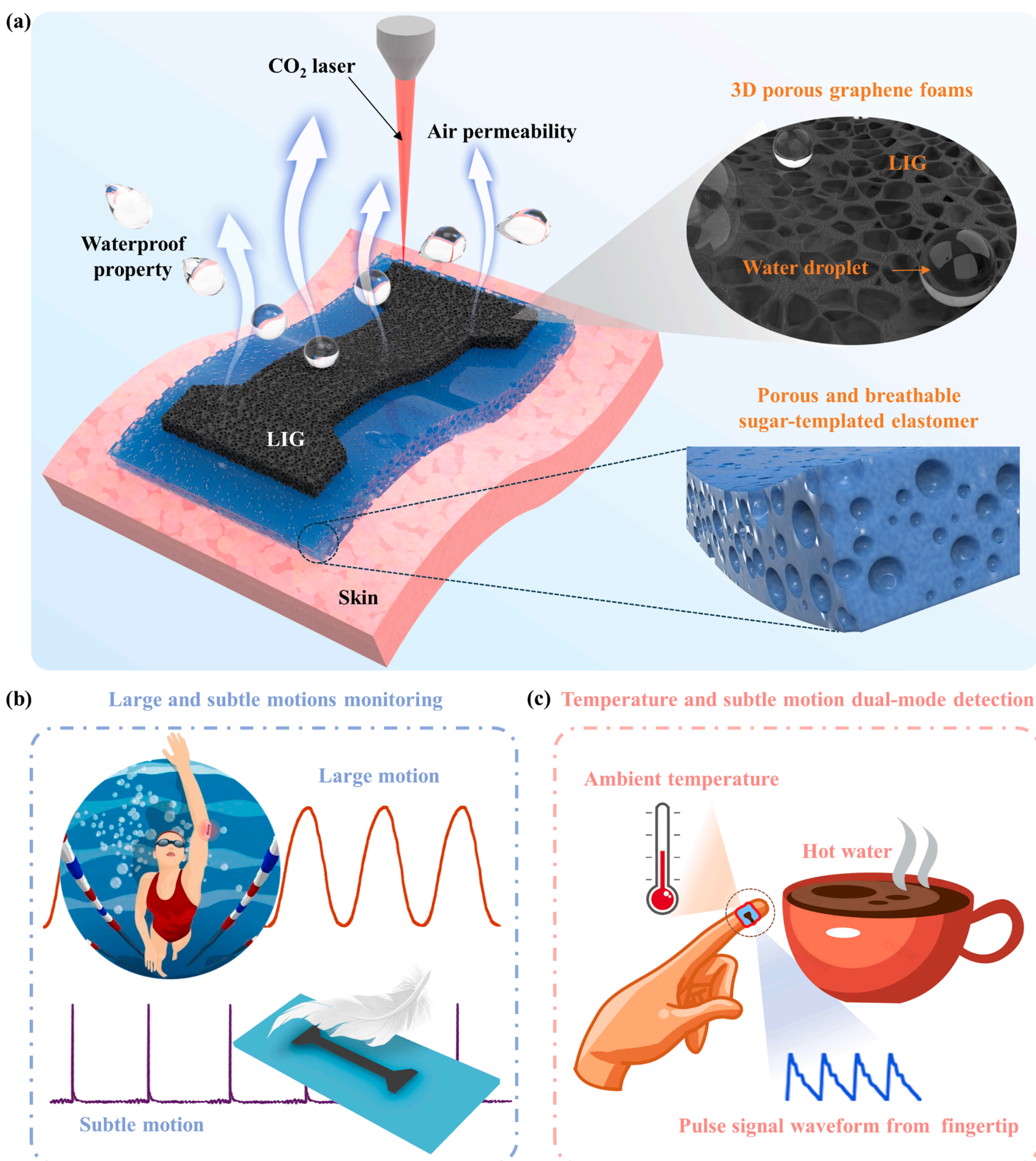

Fig. 1. Schematic diagram showing (a) the preparation, structure, and (b, c) application of waterproof dual-mode sensors for detecting large, small, and even subtle motions and temperature variations in both dry and underwater conditions.

air and moisture permeability of the sensor is introduced by the porous and breathable sugar-templated elastomer for an improved level of comfort with no skin alterations (Fig. 1**a**). Besides functioning in dry conditions, the waterproof property of the sensor further allows the sensor to accurately monitor the large, small, and even subtle motions and temperature variations in both dry and underwater conditions (Fig. 1**b, c**).

2.2. Structural, Material, and mechanical characterization of the Dual-Mode sensor

The scanning electron microscope (SEM) images of the surface and cross-section of the porous LIG foam orderly formed microstructures along the laser scribing direction with a line width of ~127 μm (comparable to the laser spot diameter[20,35]) (Fig. 2**a**). The high porosity in the crumpled 3D graphene networks formed from the release of gaseous products facilitates the infiltration of the PDMS prepolymer. The resulting LIG/PDMS composite exhibits reduced surface roughness

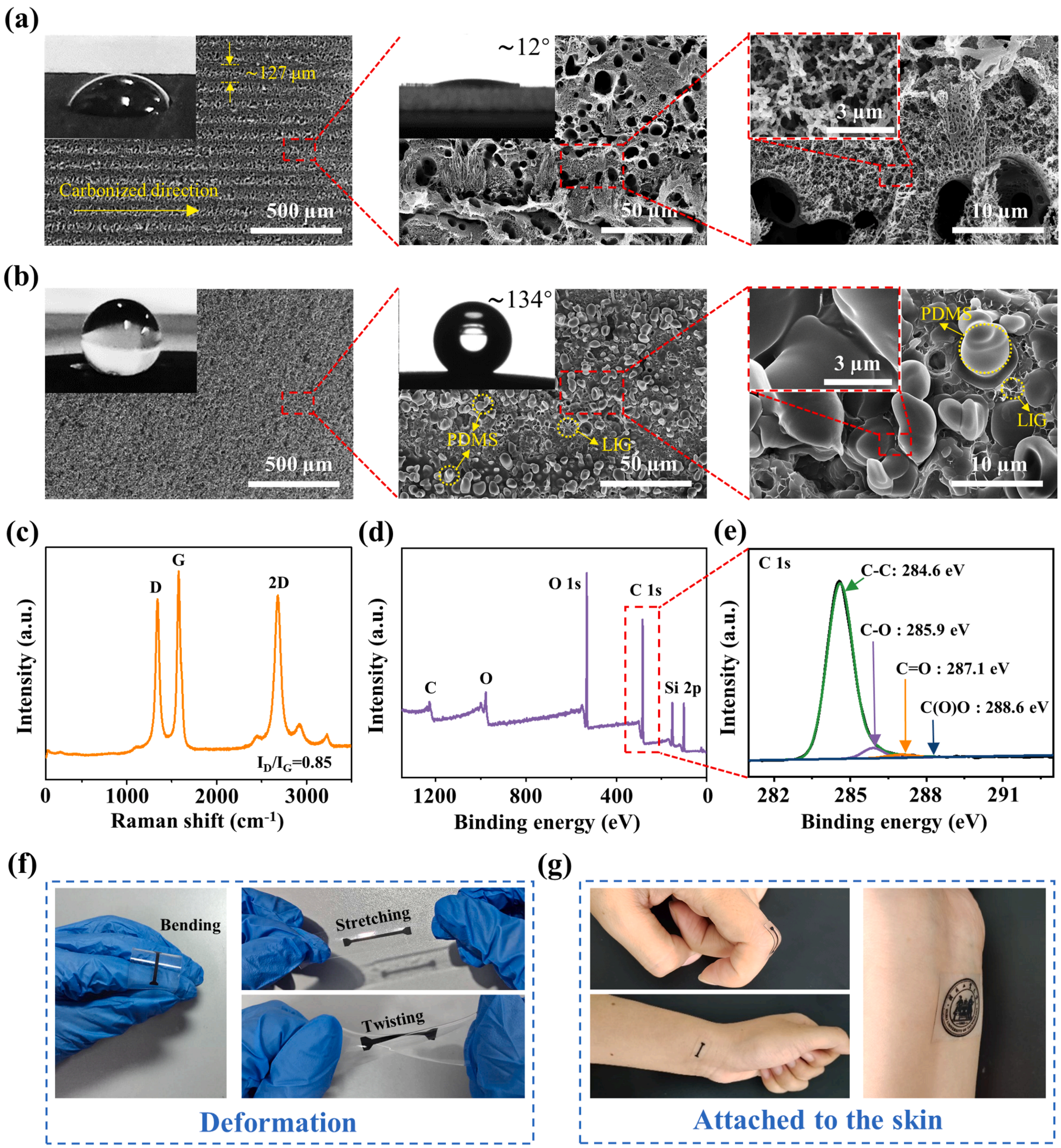

Fig. 2. Structural, material, and mechanical characterizations of the dual-mode sensor. SEM images of (a) the LIG and (b) LIG/PDMS composite at different magnifications, with the water contact angle measured to be 12° and 134°, respectively. (c) Raman spectra and (d) XPS survey spectra of the LIG/PDMS composite with the deconvoluted peaks shown in the inset. Photographs of the sensor (f) under deformation (e.g., bending, stretching, and twisting) and (g) on varying locations of the skin (e.g., finger, wrist, and arm).

(Fig. 2b). In contrast to the superhydrophilic LIG with polar hydroxyl and epoxy groups grafted the surface (contact angle of 12°)[36], the LIG/PDMS composite is hydrophobic with a contact angle of 134° (due to the hydrophobic PDMS). The cross-sectional view of the LIG/PDMS composite after transfer shows an interconnected 3D structure of multilayered graphene flakes with a thickness of ca. 50 μm (Figure S3).

Characterizations of the lattice defects, constituent elements, and content of the graphene layer have been made with the Raman and X-ray photoelectron spectroscopy (XPS) spectra. The Raman spectra of the LIG/PDMS exhibit three characteristic peaks (Fig. 2c): 1) the G peak at 1580 cm^{-1} from the vibration of carbon atoms with sp^2 hybridization in the 2D hexagonal lattices, 2) the D peak at 1350 cm^{-1} suggesting abundant graphene edges and disordered graphene structures, and 3) the 2D peak at 2680 cm^{-1} indicating a multilayered structure. A

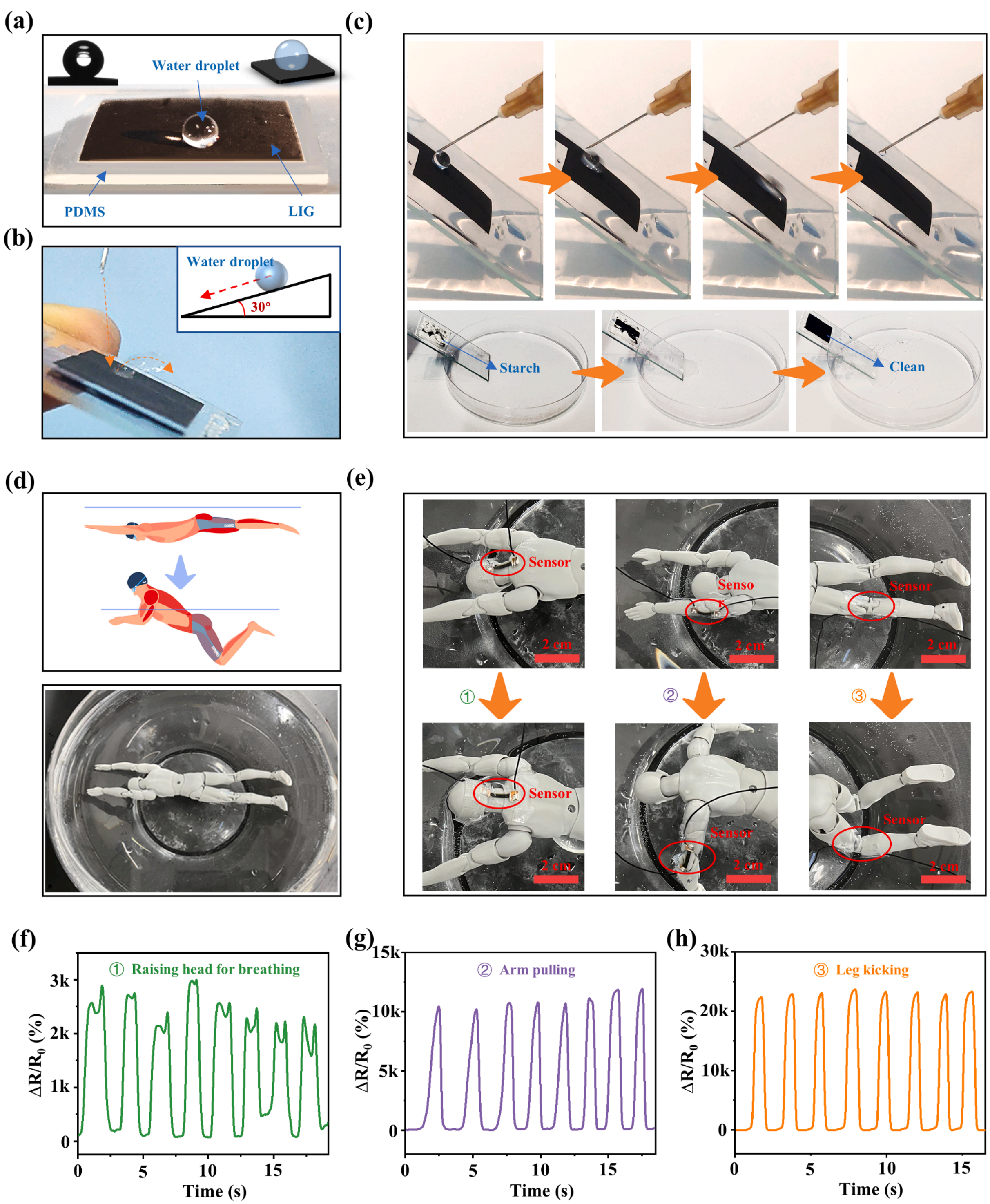

Fig. 3. Water-resistant and self-cleaning performance the sensor. Optical images of the LIG/PDMS composite sensor (a) with a water droplet statically placed on top or (b) subjected to dynamic motion of water droplets (incline angle of 30°). (c) Rolling of the water droplet on the LIG/PDMS surface cleans the sensor surface contaminated by starch. (d) Schematic and optical image showing the sensor on the swimmer to (e) detect underwater motions during breaststroke, with corresponding real-time sensor responses during (f) raising head for breathing, (g) arm pulling, and (h) leg kicking.

relatively large ratio I_D/I_G of 0.85 confirms the presence of few-layered porous graphene and a reasonable number of defects in LIG/PDMS, which is consistent with the previous results[37]. The chemical composition of the composite revealed by high-resolution XPS spectra indicates the presence of C, O, and Si, as well as the absence of N (Fig. 2**d**, **Figure S4**). The deconvoluted peaks of the most significant C 1 s region in the XPS spectra (Fig. 2**e**) show the distinct C–C peak centered at 284.6 eV for the graphitic structure. Together with the considerably reduced C-O, C = O, and C(O)O components, the results reveal the dominated sp^2 carbons and broken chemical bonding for high-quality LIG.

The easily removed LIG/PDMS composite from the PI substrate could

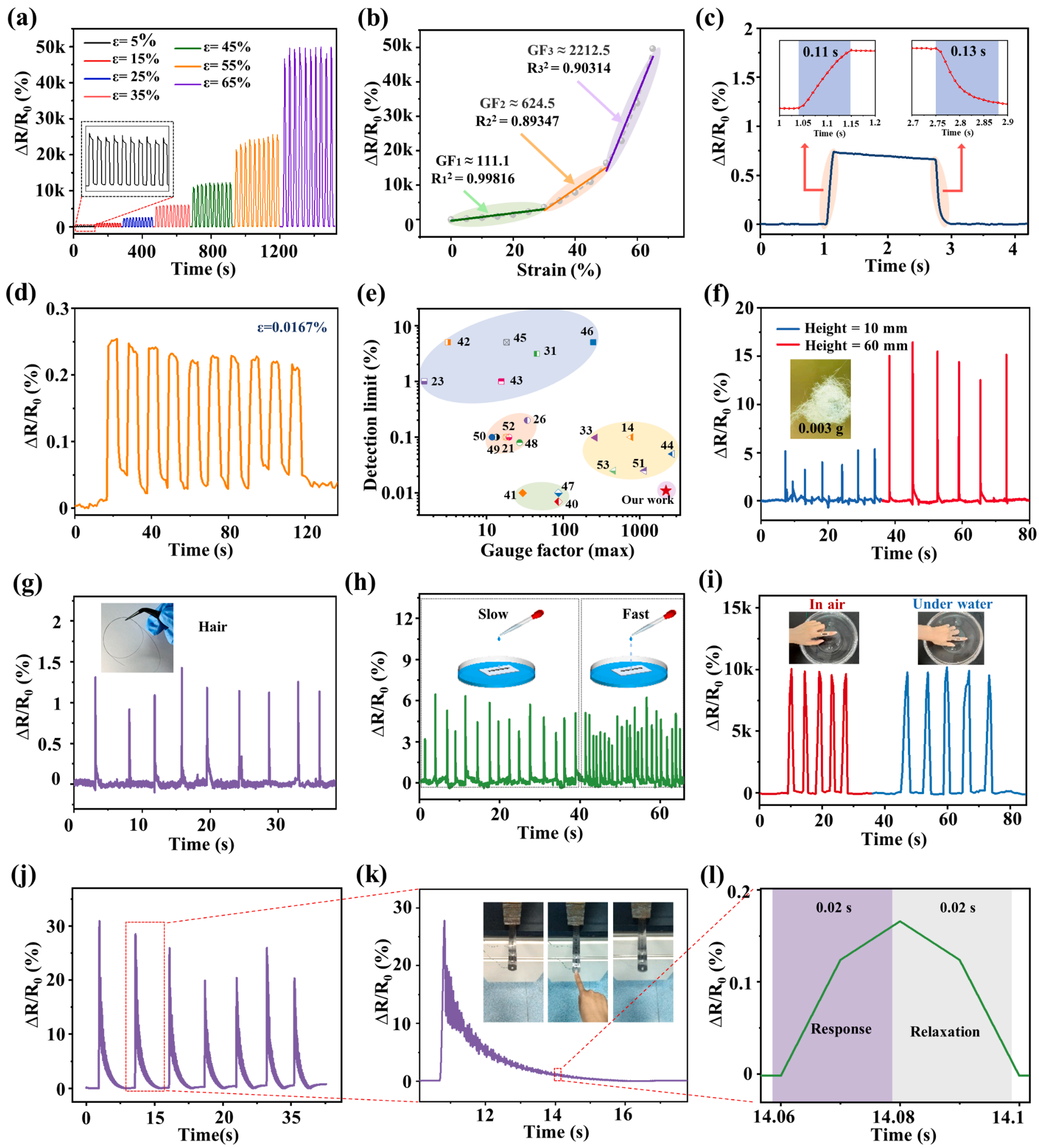

Fig. 4. Characterization of the strain sensing performance of the dual-mode sensor. Relative resistance variation as a function of (a) time and (b) strain for a tensile strain in the range of 5 to 65%, from which the sensitivity or gauge factor (GF) is calculated. (c) The representative curve for determining the response and relaxation rates. (d) The sensor response to a cyclic strain between 0 and 0.0167%. (e) Comparison in the strain detection limit and gauge factor highlighting the superior performance of this work. Sensor responses to the shock wave created (f) by 0.003 g cotton falling from the height of 10 mm and 60 mm or (g) by a hair. (h) Detection of the vibration wave from the falling water droplets with the sensor suspended on/in the water (height of 10 cm). (i) Comparison in the sensing performance between the in-air and underwater detections of the same hand gesture. (j) Recognition of signals under damped vibration and (k) zoom-in view of the single shock with photographs showing the setup. (l) Measurements of the response and relaxation time in response to the damped vibration.

be easily deformed (upon folding, stretching, or twisting) (Fig. 2**f**) or attached to varying locations of the human body (e.g., finger joint, wrist, or arm) (Fig. 2**g**). The facile control of the laser direct writing process can also generate programmed patterns with resistance (e.g., university emblem pattern in Fig. 2**g**).

2.3. Waterproof performance and swimming styles monitoring of the Dual-Mode sensor

The as-prepared hydrophobic LIG/PDMS composite with a water contact angle of 134° can repel the water in both the static (Fig. 3**a**) and dynamic conditions (off an incline with an angle of 30°, Fig. 3**b**, **Video S1**). The water droplet easily rolling off the sensor surface can also provide the self-cleaning capability to remove the dusk or contaminant such as starch (Fig. 3**c**). The integration of the sensor with a wireless transmission and powering module (BIOSYS intelligent sensing system) allows the integrated device system to monitor the underwater movements with a smartphone (**Figure S5**). The excellent waterproof property of the dual-mode sensor allows it to be used on swimmers (Fig. 3**d**) to detect varying movements and motions during breaststroke (Fig. 3**e**). In particular, the motion and frequency of raising the head for breathing, arms pulling, and leg kicking can be detected with the sensor on the neck, elbows, and knees to monitor the corresponding bending at these locations (Fig. 3**f-h**).

2.4. Strain sensing performance of the Dual-Mode sensor

The current–voltage (*I-V*) curves of the dual-mode sensor upon varying tensile strains from 0 to 65% exhibit a linear relationship to confirm the Ohmic behavior (**Figure S6a**). As the strain increases, the slope of the *I-V* curve decreases due to the increased resistance, confirming the piezoresistive characteristic of the LIG/PDMS composite. The *I-V* curve becomes almost flat for tensile strains higher than 65%, indicating the vanishing conductive pathways. The sensor response to stepwise increased tension strain loading, followed by unloading, is almost symmetric (**Figure S6b**) to indicate reversibility and low hysteresis (**Figure S6c**). Although the stress–strain curves of the dual-mode sensor indicate the maximum stretchability of 83% before the break (**Figure S6d**), the tensile strain is only applied up to 65% in the following investigations to avoid potential damage.

The electromechanical performance of the dual-mode sensor relates the relative resistance change ($\Delta R/R_0$, %) with the engineering tensile strain, $\varepsilon=(L-L_0)/L_0$, where L_0 and L are the lengths before and after stretching. The slope in the curve of the relative resistance change versus the engineering tensile strain gives the sensitivity or gauge factor (GF) of the strain sensor, i.e., $GF=(\Delta R/R_0)/\varepsilon$ [38].

The sensor response is highly repeatable for the applied tensile strain from 5 to 65% (Fig. 4**a**). In the strain range up to 65%, the calibration curve is piecewise linear in three regions with reasonably high GF: 111.1 for strain 0–30%, 624.5 for strain 30–50%, and 2212.5 for strain 50–65% (Fig. 4**b**). While large GF is often preferred, the overlarge GF also leads to reduced accuracy in the measured strain (e.g., the error can be 50% for a GF of 5×10^4) [39]. Therefore, the GF of the dual-mode sensor from this work falls into the desirable range to ensure measurement accuracy. The strain sensor can also rapidly respond to the loading/unloading cycles with a response time of 0.11 s and recovery time of 0.13 s (Fig. 4**c**).

Besides the high sensitivity and measurement accuracy, the dual-mode sensor has a salient feature of detecting subtle strain levels of 0.0167, 0.05, 0.1, 0.2, and 0.4% (**Figure S6e**). The sensor response to the tiny cyclic strain of 0.0167% is highly reliable and repeatable with a signal-to-noise ratio of 48.82 (Fig. 4**d**), which indicates the limit of detection (LOD) could be much smaller to be 0.0112%. The relative resistance change at an applied strain of 0% is not vanishing because of the drift in the initial resistance from the tiny changes in the ambient environment as in the previous literature reports[40,41]. The dual-mode strain sensor with combined ultralow LOD and high sensitivity compares favorably with previous literature reports (Fig. 4**e**) [14,21,23,26,31,33,40–53]. The combined advantages of the dual-mode sensor allow it to detect the tiny deformation or impact from falling of the 0.003 g cotton (Fig. 4**f** and **Video S2**) or hair (Fig. 4**g** and **Video S3**). The water-resistant property of the sensor further allows it to be freely suspended on/in the water and detect small vibration waves generated by the water droplets impacting the water surface from a height of 10 cm (Fig. 4**h** and **Video S4**). The sensor performance is negligibly affected by the presence of water, as demonstrated in the comparison between in-air and underwater responses to the same hand gesture (Fig. 4**i**) or finger bending (**Video S5**).

Because of the varied frequencies in different motions or human activities, the dual-mode sensor is verified to respond to a cyclic strain of 5% at a frequency from 0.2 to 1.0 Hz (**Figure S6f**). Attaching the sensor to an oscillating steel ruler provides the characterization of the sensitivity and response time at different frequencies and amplitudes (Fig. 4**j, k**). The recognition signal promptly revealed a damped vibration of the ruler with a response time of 0.02 s (Fig. 4**l** and **Video S6**), which is sufficient for detecting human motion. Generally, mechanical stimuli occurring at a higher speed results in a smaller response time [54]. The ultrafast response, superb sensitivity, and ultralow detection limit enable the dual-mode sensor to detect various physical vibrations in the local environment. The long-term electromechanical stability of the sensor is confirmed over 15,000 stretching/releasing cycles for a strain of 5% (**Figure S7a**), 30% (**Figure S7b**), and 60% (**Figure S7c**), which can prepare the sensor for highly reliable long-term use.

The waterproof property of the sensor also exhibits stability over time. With the sensor placed 50 cm from the bottom surface of the container (**Figure S8a**), it can accurately capture the dynamic wave caused by water droplets falling on the water surface over 24 h (with water emptied every 8 h, **Figure S8b**). The steady rise in the water level in each 8-hour cycle leads to reduced wave vibration and signal in the sensor (**Figure S8a**), providing a method for water level detection. The average responses over 30 min in the initial, middle, and end of each 8-hour cycle exhibit reasonably good accuracy and stability with the sensor underwater for 24 h (**Figure S8c**). The monitoring of underwater finger bending over 7 days (**Figure S9**) also shows a small response variation (9.9%) (**Figure S10**), demonstrating the long-term stability of the sensor.

The wide working strain range allows the dual-mode sensor to detect both small and large motions (30–65%), including bending motions of the finger (**Figure S11a**), wrist (**Figure S11b**), and knee joints (**Figure S11c**) at different angles and frequencies for potential applications in rehabilitation. Furthermore, the sensors placed on five finger joints can differentiate hand gestures (e.g., a, b, c, d, and ok) to detect sign language and facilitate communication for people with language disorders (**Figure S12**).

Even smaller human motions can be accurately detected by the highly sensitive LIG/PDMS sensor. The examples include the identification of swallowing (**Figure S13a**), chewing (**Figure S13b**), and smiling (**Figure S13c**), when attaching the sensor to the occlusal muscle, throat, and corners of the mouth, respectively. The large responses of more than 40% confirm the large sensitivity and high-fidelity sensing of these small muscle movements. Attaching the sensor on the eyelid can further monitor blink rate and prevent various eye diseases such as dry eye syndrome caused by fatigue such as from long-term computer use (**Figure S13d**). While the blink rate decreases from 30 $\min^{-1}$ in normal conditions (0–18 s area) to 12 $\min^{-1}$ in working conditions, the rapid increase to 87 $\min^{-1}$ results from the overuse of the eyes. As different words are associated with varying amplitudes and durations of the motion form from the vocal muscle [55], it is possible to differentiate the spoken words (e.g., apple, banana, yes, water, thank you) from the highly repeatable signal patterns (**Figure S14**).

The sensor based on the LIG/PDMS composite with a thin geometry (0.30 mm) and small footprint (20 mm $\times$ 10 mm) causes no irritation, itching, or any discomfort even after use for 6 days (**Figure S15a**). However, the wrist beneath the sensor becomes slightly pale after 4 days, likely due to the moisture accumulation from the skin respiration. To improve the air and moisture permeability of the sensor, the PDMS layer is replaced by a porous and breathable sugar-templated elastomer for an improved level of comfort with no skin alterations (e.g., irritation, itching, or paling) over 6 days (**Figure S15b**). According to ASTM E96-95, the breathability can be evaluated by the weight change of the bottle covered by varying films with 40 g of Silica gel desiccant inside (**Figure S16a**). The much larger weight change from the bottom covered by the porous sugar-templated elastomer than that from PDMS (**Figure S16b)** indicates much higher air and moisture permeability for excellent vapor rate and improved level of comfort. The underwater performance evaluation of the sensor based on the sugar-templated elastomer shows comparable results between in-air and underwater applications to large finger bending of ca. 30° (**Figure S17a**). The sensor can also detect small yet rapid vibration waves generated by a water droplet falling on the water surface from a height of 10 cm (**Figure S17b**). The weak human pulses can also be detected by the sensor based on the sugar-templated elastomer in air and underwater (**Figure S17c**).

2.5. Temperature sensing performance of the Dual-Mode sensor

The characterization of the temperature sensing performance of the dual-mode sensor is obtained by using a 20 × 20 mm^2 Peltier module for a stable temperature (**Figure S18**). The temperature-dependent *I-V* curves for the temperature ranging from 10 to 185 °C (**Figure S19a**) provide the relative resistance changes of the dual-mode sensor as a function of the temperature (Fig. 5a). From the nearly linear relationship between the relative resistance change and temperature, the temperature coefficient of resistance (TCR) is caculated as 0.97 × 10^{-2} $°C^{-1}$, which is consistent than the literature reports. Although electron–phonon scattering in the graphene gives a negative TCR [56,57], the mismatch in the coefficient of thermal expansion (CTE) between LIG and PDMS causes interparticle-dependent transport mechanisms to give a positive TCR [24]. The reversible response in the temperature sensor allows it to rapidly respond to temperature changes over 100 °C in both dynamic and cyclic tests (Fig. 5b and **Figure S19b**). Besides a large working range, the temperature sensor with a high resolution can accurately detect the cyclic ambient temperature changes within 0.2 °C, indicating a much higher resolution (Fig. 5c). As a result, the LIG/PDMS sensor can easily and reliably detect heating and cooling cycles with a

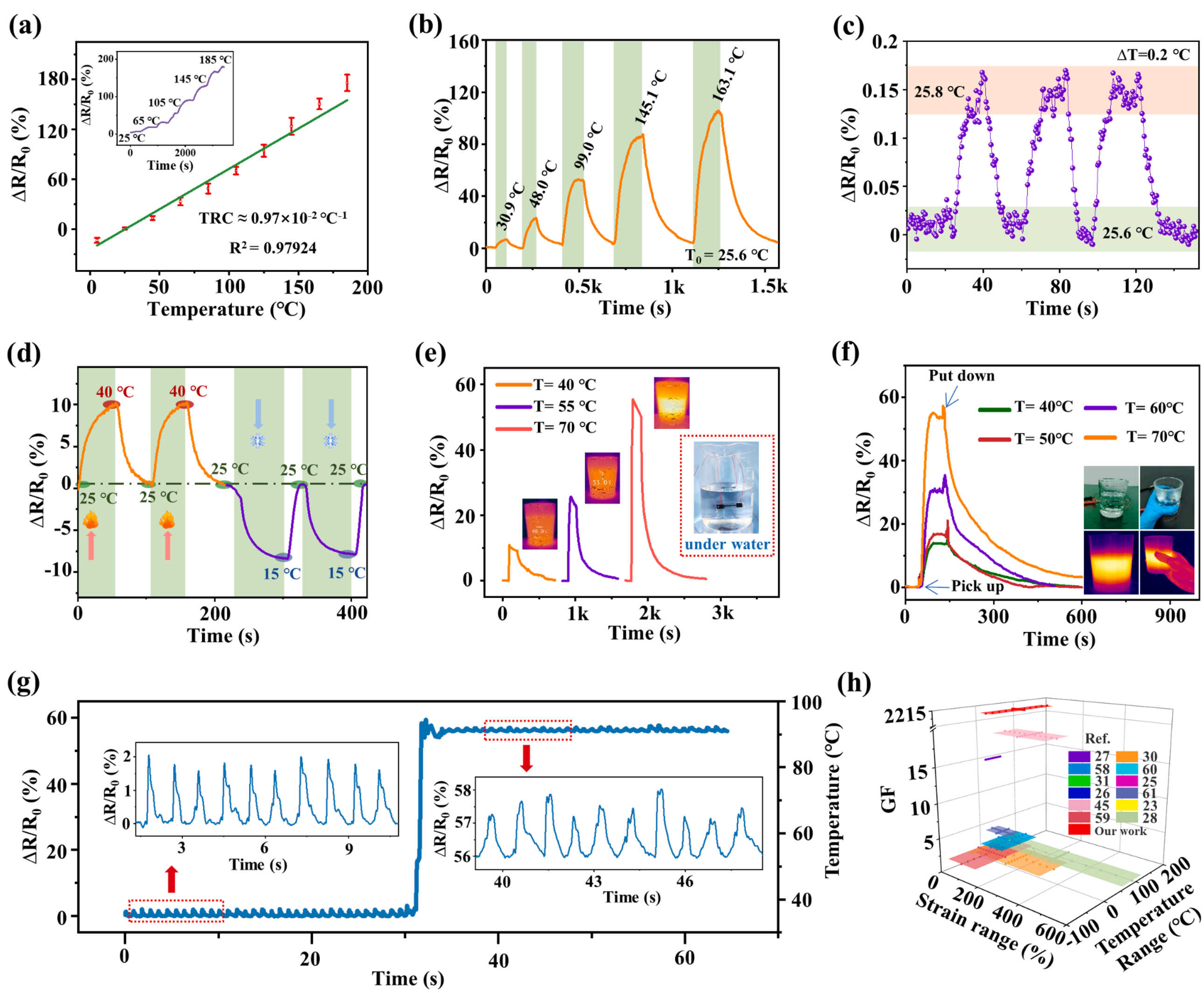

Fig. 5. The temperature sensing performance of the dual-mode sensor. Normalized relative resistance changes ($\Delta R/R_0$, %) of the dual-mode sensor as a function of (a) temperature from 10 to 185 °C and (b) time. Variations in the relative resistance (c) for a differential temperature change ΔT of 0.2 °C and (d) for various heating–cooling cycles. (e) Dynamic response of underwater sensors to different water temperatures. (f) Sensor responses during picking up and putting down the cup at different temperatures with the optical and infrared images shown in the inset. (g) Simultaneous, real-time monitoring of skin temperature and pulse. (h) Comparison of sensor dual-mode performance with other literature.

much larger temperature change (Fig. 5d).

Attaching the sensor to the human skin below the nose can also detect the skin temperature and respiration from the temperature variations (Figure S19c). The sensor can also measure breathing patterns (Figure S19d), forehead temperature (orange), axillary temperature (purple) (Figure S19e), and the human skin surface temperature (Figure S19f). The excellent waterproof performance also allows the sensor to be placed on the inner wall of the water cup for dual-mode sensing underwater (Fig. 5e). For instance, heating the water to a prescribed temperature (e.g., 40, 55, or 70 °C) is indicated by the stabilized sensor response after the rapid increase. Next, emptying the cup results in a rapid temperature decrease, as evidenced by the delay to a vanishing value in the sensor response. The recovery times are longer than the response times due to the slow heat dissipation inside the cup.

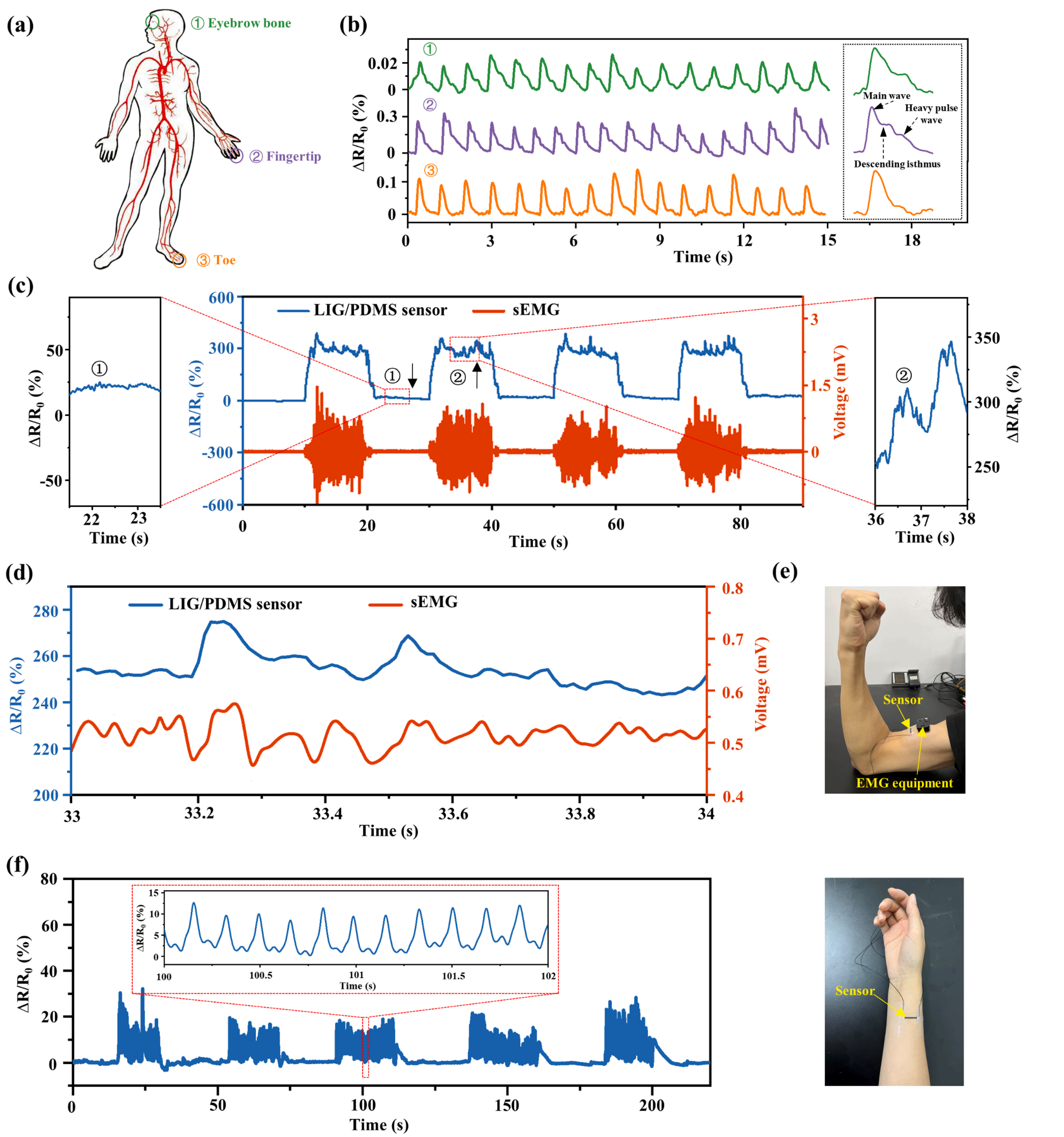

Fig. 6. Monitoring of subtle human signals. (a) Schematic showing the network of human arteries with the most subtle motions on the eyebrow bone, fingertip, and toe (furthest from the heart are). (b) Measurements of the pulse waveform from the eyebrow bone (green), fingertip (purple), and toe (orange). (c) The comparison between the sensor response (blue) and the muscle action potential obtained by the surface electromyogram (sEMG) (red) in response to multiple voluntary relaxing/contracting cycles of the biceps muscle group, with a zoom-in view of the sensor response under muscle relaxation and contraction. (d) The comparison of the sensor response (blue) and sEMG signals (red) processed with a built-in data processing system within a period of 1 s. (e) Fixing the sensor on the biceps measures the signal of muscle tension. (f) The sensor response to the simulated Parkinson's static tremor at a frequency of 5.5 Hz with an optical image showing the sensor placement.

2.6. Applications of the Dual-Mode sensor

The dual-mode sensor as a soft, wearable interface can easily capture multiple stimuli in varying applications. As a demonstration for human–machine interfaces or human-robot collaborations with a requirement for complex missions, the dual-mode sensor is applied to the water filling and drinking process (Fig. 5**f**). After picking up the empty cup at 50 s (room temperature of 25 °C), hot water of different temperatures from 35 to 65 °C is poured into the cup, as indicated by the rapid temperature increase to a plateau corresponding to each temperature. Next, emptying the cup (for simulated drinking) is captured by the flat curve, followed by putting down the cup as signaled by the peaks in the relative resistance changes at 150 s. The difference in the sensor response to subtle strain and large temperature variations can also be used to simultaneously monitor the human pulse signal and heat stress when attached to the wrist (Fig. 5**g**). The rhythmic relative resistance changes correspond well to the pulse signals, whereas the sudden large change in the relative resistance around the time of 32 s signals the slowly approaching hot water cup that simulates the heat stress. It is important to note that the pulse wave can still be accurately detected after the sensor response to temperature quickly stabilizes. The dual-mode sensor can decouple strain and temperature input signals when they are applied in sequence (Fig. 5**f**) or when their resulting relative resistance changes have a significant difference in magnitude (Fig. 5**g**). Although it is often challenging for the dual-mode sensor to simultaneously decouple two input signals, the thermoelectric effect of laser-induced graphene could be exploited to generate two outputs (i.e., slopes and intercepts in the current–voltage curves). The dual-mode sensor with high (piecewise) linearity and sensitivity (e.g., GF = 2212.5) over a broad strain (0.0167–65%) and temperature range (10–185 °C) compares favorably with the previous literature reports (Fig. 5**h**)[23,25–28,30,31,45,58–61].

2.7. Monitoring of subtle human signals

The ultralow detection limit of the sensor to tiny strain levels provides the sensor with the unique capability to detect subtle skin deformations/movements such as pulse, facial micro-expression, and epidermal nerve twitch. The detection of pulse waveforms can go beyond the common locations such as the neck carotid artery (**Figure S20a**), wrist artery (**Figure S20b** and **Videos S7**), and ankle (**Figure S20c**) to much more challenging locations that are farther away from the heart (Fig. 6**a**). In fact, our dual-mode sensor can still accurately detect the subtle pulse signal waveforms from eyebrow bone (green), fingertip (purple), and toe tip (orange) (Fig. 6**b**, **Video S8**). These pulse signal waveforms all exhibit the three main characteristic peaks (i.e., main wave, descending isthmus, and heavy pulse wave) to provide clinical insights for the diagnosis of cardiovascular and cerebrovascular diseases. The heartbeat frequency of 66 beats/min measured by our sensor is also consistent with the value of 67 beats/min obtained by the commercial instrument (HEM-6131, Omron). Combining the ultralow detection limit and excellent waterproof performance of the sensor, the pulse signal underwater is clearly monitored as shown in **Video S9**.

The subtle yet rapid skeletal muscle motions produced by recurrent nerve stimulations can also be captured by our dual-mode sensor (Fig. 6**e**). Our sensor exhibits instant response to the multiple cycles of voluntary contraction and relaxation in the biceps and flexor carpi radialis, with the response correlating with the surface electromyogram (sEMG) in terms of contracting periods and ranges (Fig. 6**c-e**, **Figure S21**). In particular, contraction in the biceps results in a large overall sensor response of 300 with local variations from 250 to 350. These local distinctive peaks within the response envelope in our sensor have a frequency around 15 Hz, which is consistent with that from the sEMG (Fig. 6**d**). The sEMG linear envelope processed by a standard algorithm to provide the interpretation of the mechanical activity of muscle fibers also exhibits similar major waveform patterns as captured by our sensor. Simply attaching the sensor to the forearm of the human subject can also provide a highly sensitive and rapid response to the simulated resting tremor (frequency of 3–6 Hz) for Parkinson's disease in the elderly (Fig. 6**f**). The simulated 'pill-rolling' behavior of the thumb at a frequency of 5.5 Hz is clearly identified by the subtle movement detection from the radial wrist flexor muscle.

3. Conclusion

In summary, this work reports a highly sensitive and reliable, waterproof dual-mode sensor based on the LIG/PDMS composite for strain and temperature detection. The sensor with a large sensitivity over a wide range of temperature and tensile strain, fast response, and excellent stability can accurately detect large, small, and even subtle human motions and temperature variations. The waterproof property of the dual-mode sensor further provides the sensor with self-cleaning and waterproof capabilities for detecting temperature and motion underwater. The results and demonstrations presented in this work pave the way in multifunctional soft electronics for applications in human–computer interaction, health monitoring and early disease prevention, and personalized medicine.

4. Experimental section

4.1. Materials

Polyimide (PI) film with a thickness of 75 μm was purchased from Suzhou Dongxuan plastic products Co. Ltd (Jiangsu, China). Peltier elements with area 20 × 20 mm was purchased from Taifengfa electronics Co. Ltd (Shenzhen, China). The water-soluble tape was supplied by the Yongri adhesive Co. Ltd. (Shanghai, China). The PDMS (Sylgard 184 Silicone Elastomer) were purchased from Dow Corning Corporation (U. S.A).

4.2. Fabrication of the Dual-Mode sensor

A piece of the polyimide film with the thickness of 75 μm was attached to a glass substrate by water-soluble tape to provide handling rigidity during the process. The PI film was carbonized with a computer-designed layouts (consisting of a 15 mm × 1.25 mm rectangular sensing region and two trapezoidal electrodes) by a CO_2 laser (power of 6.9 W, scanning speed of 355.6 mm s^{-1}, scanning gap of 0.1 mm, and raster mode). The PDMS solution was prepared at room temperature with stirring using 1 g of prepolymer (a) and 0.1 g of crosslinking agent (b) in a mass ratio of 10:1. Then, the PDMS solution was poured onto the laser-treated PI film after curing at 85 °C for 2 h. Subsequently, the PDMS film was peeled off from the PI film. Thus, the porous graphene layer was transferred to the flexible PDMS film with reserved patterns, completing the dual-model sensor fabrication.

4.3. Fabrication of the sensor based on the Sugar-Templated elastomer

After adding and mixing 1 g of sugar powders with 0.5 g of PDMS solution by stirring, the mixed PDMS/sugar solution was cured on the laser-treated PI film at 85 °C for 2 h. Peeling off the PI was followed by dissolving the sugar to complete the transfer process. The thickness and porosity of the sugar-templated elastomer can be controlled by the coated thickness of the PDMS/sugar mixture and the grain size of the sugar powder, respectively.

4.4. Characterizations

SEM images were collected by a field emission scanning electron microscope (JSM 7100F, JEOL). Raman shifts were obtained by laser micro Raman spectrometer (inVia Reflex, Renishaw). X-ray photoelectron spectroscopy (XPS) spectra were measured using a ESCALAB 250 photoelectron spectrometer (ESCALAB 250Xi, Thermo Fisher Scientific). Contact Angle images were obtained by a fully automatic contact angle measuring system (DSAHT, KRUSS GmbH).

4.5. Testing of Dual-Mode sensors

A moving fixture (JSV-H1000, Japan Instrumentation System Co., Ltd.) and force gauge (HF-1, Japan Instrumentation System Co., Ltd.) in combination with home-made clampers were used to apply longitudinal tensile strain. The electromechanical properties of the dual-modal sensors were determined using a two-point measurement with a digital source meter (Keithley 2400, Tektronix, U.S.A.) at a constant voltage of 0.05 V. The temperature of sensor in the was measured by an infrared camera (Ti32, FLUKE, U.S.A).

Declaration of Competing Interest

The authors declare that they have no known competing financial interests or personal relationships that could have appeared to influence the work reported in this paper.

Acknowledgements

This work was supported by the National Natural Science Foundation of China (51705126, 61871173), and the Key Research and Development Project of Hebei Province (20271701D, 21372002D). H.C. acknowledges the supports provided by the National Science Foundation (NSF) (Grant No. ECCS-1933072), the National Heart, Lung, And Blood Institute of the National Institutes of Health under Award Number R61HL154215, and Penn State University.

Appendix A. Supplementary data

Supplementary data to this article can be found online at https://doi.org/10.1016/j.cej.2022.136631.

References

[1] Y. Song, D. Mukasa, H. Zhang, W. Gao, Self-powered wearable biosensors, Acc. Mater. Res. 2 (3) (2021) 184–197, https://doi.org/10.1021/accountsmr.1c00002.

[2] Y. Niu, H. Liu, R. He, Z. Li, H. Ren, B. Gao, H. Guo, G.M. Genin, F. Xu, The new generation of soft and wearable electronics for health monitoring in varying environment: From normal to extreme conditions, Mater. Today. 41 (2020) 219–242, https://doi.org/10.1016/j.mattod.2020.10.004.

[3] G. Lee, J.H. Son, S. Lee, S.W. Kim, D. Kim, N.N. Nguyen, S.G. Lee, K. Cho, Fingerpad-inspired multimodal electronic skin for material discrimination and texture recognition, Adv. Sci. 8 (9) (2021) 2002606, https://doi.org/10.1002/advs.202002606.

[4] Y.H. Jung, J.H. Kim, J.A. Rogers, Skin-integrated vibrohaptic interfaces for virtual and augmented reality, Adv. Funct. Mater. 31 (39) (2020) 2008805, https://doi.org/10.1002/adfm.202008805.

[5] F. Ershad, A. Thukral, J. Yue, P. Comeaux, Y. Lu, H. Shim, K. Sim, N.I. Kim, Z. Rao, R. Guevara, L. Contreras, F. Pan, Y. Zhang, Y.S. Guan, P. Yang, X. Wang, P. Wang, X. Wu, C. Yu, Ultra-conformal drawn-on-skin electronics for multifunctional motion artifact-free sensing and point-of-care treatment, Nat. Commun. 11 (1) (2020) 3823, https://doi.org/10.1038/s41467-020-17619-1.

[6] J.R. Sempionatto, M. Lin, L.U. Yin, E. De la paz, K. Pei, T. Sonsa-ard, A.N. de Loyola Silva, A.A. Khorshed, F. Zhang, N. Tostado, S. Xu, J. Wang, An epidermal patch for the simultaneous monitoring of haemodynamic and metabolic biomarkers, Nat Biomed Eng 5 (7) (2021) 737–748.

[7] H.U. Chung, A.Y. Rwei, A. Hourlier-Fargette, S. Xu, K. Lee, E.C. Dunne, Z. Xie, C. Liu, A. Carlini, D.H. Kim, D. Ryu, E. Kulikova, J. Cao, I.C. Odland, K.B. Fields, B. Hopkins, A. Banks, C. Ogle, D. Grande, J.B. Park, J. Kim, M. Irie, H. Jang, J. Lee, Y. Park, J. Kim, H.H. Jo, H. Hahm, R. Avila, Y. Xu, M. Namkoong, J.W. Kwak, E. Suen, M.A. Paulus, R.J. Kim, B.V. Parsons, K.A. Human, S.S. Kim, M. Patel, W. Reuther, H.S. Kim, S.H. Lee, J.D. Leedle, Y. Yun, S. Rigali, T. Son, I. Jung, H. Arafa, V.R. Soundararajan, A. Ollech, A. Shukla, A. Bradley, M. Schau, C. M. Rand, L.E. Marsillio, Z.L. Harris, Y. Huang, A. Hamvas, A.S. Paller, D.E. Weese-Mayer, J.Y. Lee, J.A. Rogers, Skin-interfaced biosensors for advanced wireless physiological monitoring in neonatal and pediatric intensive-care units, Nat. Med. 26 (3) (2020) 418–429, https://doi.org/10.1038/s41591-020-0792-9.

[8] L. Yang, H. Wang, W. Yuan, Y. Li, P. Gao, N. Tiwari, X. Chen, Z. Wang, G. Niu, H. Cheng, Wearable Pressure sensors based on mxene/tissue papers for wireless human health monitoring, ACS Appl. Mater. Interfaces. 13 (50) (2021) 60531–60543, https://doi.org/10.1021/acsami.1c22001.

[9] H. Zhang, W. Han, K. Xu, Y. Zhang, Y. Lu, Z. Nie, Y. Du, J. Zhu, W. Huang, Metallic sandwiched-aerogel hybrids enabling flexible and stretchable intelligent sensor, Nano. Lett. 20 (5) (2020) 3449–3458, https://doi.org/10.1021/acs.nanolett.0c00372.

[10] H. Zhao, Y. Zhou, S. Cao, Y. Wang, J. Zhang, S. Feng, J. Wang, D. Li, D. Kong, Ultrastretchable and washable conductive microtextiles by coassembly of silver nanowires and elastomeric microfibers for epidermal human-machine interfaces, ACS. Mater. Letters. 3 (7) (2021) 912–920, https://doi.org/10.1021/acsmaterialslett.1c00128.

[11] H. Wu, G. Yang, K. Zhu, S. Liu, W. Guo, Z. Jiang, Z. Li, Materials, devices, and systems of on-skin electrodes for electrophysiological monitoring and human-machine interfaces, Adv. Sci (Weinh). 8 (2) (2021) 2001938, https://doi.org/10.1002/advs.202001938.

[12] J.H. Lee, H. Kim, J.Y. Hwang, J. Chung, T.M. Jang, D.G. Seo, Y. Gao, J. Lee, H. Park, S. Lee, H.C. Moon, H. Cheng, S.H. Lee, S.W. Hwang, 3D Printed, customizable, and multifunctional smart electronic eyeglasses for wearable healthcare systems and human-machine interfaces, ACS Appl. Mater. Interfaces. 12 (19) (2020) 21424–21432, https://doi.org/10.1021/acsami.0c03110.

[13] Y. Qiu, Y. Tian, S. Sun, J. Hu, Y. Wang, Z. Zhang, A. Liu, H. Cheng, W. Gao, W. Zhang, H. Chai, H. Wu, Bioinspired, multifunctional dual-mode pressure sensors as electronic skin for decoding complex loading processes and human motions, Nano. Energy. 78 (2020), 105337, https://doi.org/10.1016/j.nanoen.2020.105337.

[14] Y. Cai, J. Shen, G. Ge, Y. Zhang, W. Jin, W. Huang, J. Shao, J. Yang, X. Dong, Stretchable Ti3C2Tx MXene/carbon nanotube composite based strain sensor with ultrahigh sensitivity and tunable sensing range, ACS. Nano. 12 (1) (2018) 56–62, https://doi.org/10.1021/acsnano.7b06251.

[15] H. Li, H. Zheng, Y.J. Tan, S.B. Tor, K. Zhou, Development of an ultrastretchable double-network hydrogel for flexible strain sensors, ACS Appl. Mater. Interfaces. 13 (11) (2021) 12814–12823, https://doi.org/10.1021/acsami.0c19104.

[16] Z. Cui, F.R. Poblete, Y. Zhu, Tailoring the temperature coefficient of resistance of silver nanowire nanocomposites and their application as stretchable temperature sensors, ACS Appl. Mater. Interfaces. 11 (19) (2019) 17836–17842, https://doi.org/10.1021/acsami.9b04045.

[17] Y. Jiang, Q. He, J. Cai, D. Shen, X. Hu, D. Zhang, Flexible strain sensor with tunable sensitivity via microscale electrical breakdown in graphene/polyimide thin films, ACS Appl. Mater. Interfaces. 12 (52) (2020) 58317–58325, https://doi.org/10.1021/acsami.0c19484.

[18] H.J. Kim, A. Thukral, C. Yu, Highly sensitive and very stretchable strain sensor based on a rubbery semiconductor, ACS Appl. Mater. Interfaces. 10 (5) (2018) 5000–5006, https://doi.org/10.1021/acsami.7b17709.

[19] J. Shin, B. Jeong, J. Kim, V.B. Nam, Y. Yoon, J. Jung, S. Hong, H. Lee, H. Eom, J. Yeo, J. Choi, D. Lee, S.H. Ko, Sensitive wearable temperature sensor with seamless monolithic integration, Adv. Mater. 32 (2) (2020), e1905527, https://doi.org/10.1002/adma.201905527.

[20] A. Chhetry, M. Sharifuzzaman, H. Yoon, S. Sharma, X. Xuan, J.Y. Park, MoS2-decorated laser-induced graphene for a highly sensitive, hysteresis-free, and reliable piezoresistive strain sensor, ACS Appl. Mater. Interfaces. 11 (25) (2019) 22531–22542, https://doi.org/10.1021/acsami.9b04915.

[21] C. Liu, M. Li, B. Lu, Y. Huang, Y. Zhang, P. Liu, X. Guo, Y. Ma, Y. Zhang, S. Li, W. Chen, Y. Ge, High-sensitivity crack-based flexible strain sensor with dual hydrogen bond-assisted structure for monitoring tiny human motions and writing behavior, Organic. Electronics. 88 (2021), 105977, https://doi.org/10.1016/j.orgel.2020.105977.

[22] Z. Wu, H. Ding, K. Tao, Y. Wei, X. Gui, W. Shi, X. Xie, J. Wu, Ultrasensitive, stretchable, and fast-response temperature sensors based on hydrogel films for wearable applications, ACS Appl. Mater. Interfaces. 13 (18) (2021) 21854–21864, https://doi.org/10.1021/acsami.1c05291.

[23] Y. Yan, L. Wei, X. Qiu, J. Shao, H. Liu, X. Cui, J. Huang, L. Xie, Z. Hu, C. Huang, A. Dual-Responsive, Freezing-tolerant hydrogel sensor and related thermal- and strain-sensitive mechanisms, ACS Appl. Polym. Mater. 3 (3) (2021) 1479–1487, https://doi.org/10.1021/acsapm.0c01346.

[24] A. Chhetry, S. Sharma, S.C. Barman, H. Yoon, S. Ko, C. Park, S. Yoon, H. Kim, J. Y. Park, Black Phosphorus@Laser-engraved graphene heterostructure-based temperature-strain hybridized sensor for electronic-skin applications, Adv. Funct. Mater. 31 (10) (2020) 2007661, https://doi.org/10.1002/adfm.202007661.

[25] H. Liu, H. Xiang, Z. Li, Q. Meng, P. Li, Y. Ma, H. Zhou, W. Huang, Flexible and degradable multimodal sensor fabricated by transferring laser-induced porous carbon on starch film, ACS Sustainable Chem. Eng. 8 (1) (2019) 527–533, https://doi.org/10.1021/acssuschemeng.9b05968.

[26] R. Yin, S. Yang, Q. Li, S. Zhang, H. Liu, J. Han, C. Liu, C. Shen, Flexible conductive Ag nanowire/cellulose nanofibril hybrid nanopaper for strain and temperature sensing applications, Sci. Bull. 65 (11) (2020) 899–908, https://doi.org/10.1016/j.scib.2020.02.020.

[27] H. Liu, H. Xiang, Y. Wang, Z. Li, L. Qian, P. Li, Y. Ma, H. Zhou, W. Huang, A Flexible multimodal sensor that detects strain, humidity, temperature, and pressure with carbon black and reduced graphene oxide hierarchical composite on paper, ACS Appl. Mater. Interfaces. 11 (43) (2019) 40613–40619, https://doi.org/10.1021/acsami.9b13349.

[28] J. Gu, J. Huang, G. Chen, L. Hou, J. Zhang, X. Zhang, X. Yang, L. Guan, X. Jiang, H. Liu, Multifunctional Poly(vinyl alcohol) nanocomposite organohydrogel for flexible strain and temperature sensor, ACS Appl. Mater. Interfaces. 12 (36) (2020) 40815–40827, https://doi.org/10.1021/acsami.0c12176.

[29] J. Chen, H. Wen, G. Zhang, F. Lei, Q. Feng, Y. Liu, X. Cao, H. Dong, Multifunctional conductive hydrogel/thermochromic elastomer hybrid fibers with a core-shell segmental configuration for wearable strain and temperature sensors, ACS Appl. Mater. Interfaces. 12 (6) (2020) 7565–7574, https://doi.org/10.1021/acsami.9b20612.
[30] Y. Xie, R. Xie, H.C. Yang, Z. Chen, J. Hou, C.R. Lopez-Barron, N.J. Wagner, K. Z. Gao, Iono-elastomer-based wearable strain sensor with real-time thermomechanical dual response, ACS Appl. Mater. Interfaces. 10 (38) (2018) 32435–32443, https://doi.org/10.1021/acsami.8b10672.
[31] S. Veeralingam, S. Badhulika, Bi2S3/PVDF/Ppy-Based Freestanding, Wearable, Transient Nanomembrane for Ultrasensitive Pressure, Strain, and Temperature Sensing, ACS Appl. Bio Mater. 4 (1) (2020) 14–23, https://doi.org/10.1021/acsabm.0c01399.
[32] S. Duan, B. Wang, Y. Lin, Y. Li, D. Zhu, J. Wu, J. Xia, W. Lei, B. Wang, Waterproof mechanically robust multifunctional conformal sensors for underwater interactive human-machine interfaces, Adv. Intell. Syst. 3 (9) (2021) 2100056, https://doi.org/10.1002/aisy.202100056.
[33] L. Liu, Z. Jiao, J. Zhang, Y. Wang, C. Zhang, X. Meng, X. Jiang, S. Niu, Z. Han, L. Ren, Bioinspired, superhydrophobic, and paper-based strain sensors for wearable and underwater applications, ACS Appl. Mater. Interfaces. 13 (1) (2021) 1967–1978, https://doi.org/10.1021/acsami.0c18818.
[34] Y. Liu, Z. Sheng, J. Huang, W. Liu, H. Ding, J. Peng, B. Zhong, Y. Sun, X. Ouyang, H. Cheng, X. Wang, Moisture-resistant MXene-sodium alginate sponges with sustained superhydrophobicity for monitoring human activities, Chem. Eng. J. 432 (2022) 432, https://doi.org/10.1016/j.cej.2021.134370.
[35] L. Yang, N. Yi, J. Zhu, Z. Cheng, X. Yin, X. Zhang, H. Zhu, H. Cheng, Novel gas sensing platform based on a stretchable laser-induced graphene pattern with self-heating capabilities, J. Mater. Chem. A. 8 (14) (2020) 6487–6500, https://doi.org/10.1039/c9ta07855j.
[36] S. Wang, Y. Zhang, N. Abidi, L. Cabrales, Wettability and surface free energy of graphene films, Langmuir. 25 (18) (2009) 11078–11081, https://doi.org/10.1021/la901402f.
[37] J. Lin, Z. Peng, Y. Liu, F. Ruiz-Zepeda, R. Ye, E.L. Samuel, M.J. Yacaman, B. I. Yakobson, J.M. Tour, Laser-induced porous graphene films from commercial polymers, Nat. Commun. 5 (2014) 5714, https://doi.org/10.1038/ncomms6714.
[38] W. Wang, L. Lu, Z. Li, L. Lin, Z. Liang, X. Lu, Y. Xie, Fingerprint-inspired strain sensor with balanced sensitivity and strain range using laser-induced graphene, ACS Appl. Mater. Interfaces. 14 (1) (2022) 1315–1325, https://doi.org/10.1021/acsami.1c16646.
[39] S. Li, G. Liu, L. Wang, G. Fang, Y. Su, Overlarge gauge factor yields a large measuring error for resistive-type stretchable strain sensors, Adv. Electron. Mater. 6 (11) (2020) 2000618, https://doi.org/10.1002/aelm.202000618.
[40] S. Wang, P. Xiao, Y. Liang, J. Zhang, Y. Huang, S. Wu, S.-W. Kuo, T. Chen, Network cracks-based wearable strain sensors for subtle and large strain detection of human motions, J. Mater. Chem. C. 6 (19) (2018) 5140–5147, https://doi.org/10.1039/c8tc00433a.
[41] C. Wang, K. Xia, M. Jian, H. Wang, M. Zhang, Y. Zhang, Carbonized silk georgette as an ultrasensitive wearable strain sensor for full-range human activity monitoring, J. Mater. Chem. C. 5 (30) (2017) 7604–7611, https://doi.org/10.1039/c7tc01962a.
[42] J. Huang, D. Li, M. Zhao, H. Ke, A. Mensah, P. Lv, X. Tian, Q. Wei, Flexible electrically conductive biomass-based aerogels for piezoresistive pressure/strain sensors, Chem. Eng. J. 373 (2019) 1357–1366, https://doi.org/10.1016/j.cej.2019.05.136.
[43] H. Liu, S. Zhang, Z. Li, T.J. Lu, H. Lin, Y. Zhu, S. Ahadian, S. Emaminejad, M. R. Dokmeci, F. Xu, A. Khademhosseini, Harnessing the wide-range strain sensitivity of bilayered PEDOT:PSS films for wearable health monitoring, Matter. 4 (9) (2021) 2886–2901, https://doi.org/10.1016/j.matt.2021.06.034.
[44] J. Zhou, X. Guo, Z. Xu, Q. Wu, J. Chen, J. Wu, Y. Dai, L. Qu, Z. Huang, Highly sensitive and stretchable strain sensors based on serpentine-shaped composite films for flexible electronic skin applications, Compos. Sci. Technol. 197 (2020), 108215, https://doi.org/10.1016/j.compscitech.2020.108215.
[45] G. Ge, Y. Lu, X. Qu, W. Zhao, Y. Ren, W. Wang, Q. Wang, W. Huang, X. Dong, Muscle-inspired self-healing hydrogels for strain and temperature sensor, ACS. Nano. 14 (1) (2020) 218–228, https://doi.org/10.1021/acsnano.9b07874.
[46] J.H. Pu, X.J. Zha, M. Zhao, S. Li, R.Y. Bao, Z.Y. Liu, B.H. Xie, M.B. Yang, Z. Guo, W. Yang, 2D end-to-end carbon nanotube conductive networks in polymer nanocomposites: a conceptual design to dramatically enhance the sensitivities of strain sensors, Nanoscale. 10 (5) (2018) 2191–2198, https://doi.org/10.1039/c7nr08077h.
[47] T. Huang, P. He, R. Wang, S. Yang, J. Sun, X. Xie, G. Ding, Porous fibers composed of polymer nanoball decorated graphene for wearable and highly sensitive strain sensors, Adv. Funct. Mater. 29 (45) (2019) 1903732, https://doi.org/10.1002/adfm.201903732.
[48] W. Liu, Y. Huang, Y. Peng, M. Walczak, D. Wang, Q. Chen, Z. Liu, L. Li, Stable wearable strain sensors on textiles by direct laser writing of graphene, ACS Appl. Nano Mater. 3 (1) (2020) 283–293, https://doi.org/10.1021/acsanm.9b01937.
[49] P. Puneetha, S.P.R. Mallem, Y.W. Lee, J. Shim, Strain-controlled flexible graphene/gan/pdms sensors based on the piezotronic effect, ACS Appl. Mater. Interfaces. 12 (32) (2020) 36660–36669, https://doi.org/10.1021/acsami.0c06534.
[50] L. Zhang, H. Li, X. Lai, T. Gao, X. Zeng, Three-dimensional binary-conductive-network silver nanowires@thiolated graphene foam-based room-temperature self-healable strain sensor for human motion detection, ACS Appl. Mater. Interfaces. 12 (39) (2020) 44360–44370, https://doi.org/10.1021/acsami.0c13442.
[51] Y. Yang, Z. Cao, P. He, L. Shi, G. Ding, R. Wang, J. Sun, Ti3C2Tx MXene-graphene composite films for wearable strain sensors featured with high sensitivity and large range of linear response, Nano. Energy. 66 (2019), 104134, https://doi.org/10.1016/j.nanoen.2019.104134.
[52] S. Zhang, L. Wen, H. Wang, K. Zhu, M. Zhang, Vertical CNT–Ecoflex nanofins for highly linear broad-range-detection wearable strain sensors, J. Mater. Chem. C. 6 (19) (2018) 5132–5139, https://doi.org/10.1039/c7tc05571d.
[53] Y. Liu, H. Li, M. Zhang, Wireless battery-free broad-band sensor for wearable multiple physiological measurement, ACS Appl. Electron. Mater. 3 (4) (2021) 1681–1690, https://doi.org/10.1021/acsaelm.0c01143.
[54] B. Yin, Y. Wen, T. Hong, Z. Xie, G. Yuan, Q. Ji, H. Jia, Highly stretchable, ultrasensitive, and wearable strain sensors based on facilely prepared reduced graphene oxide woven fabrics in an ethanol flame, ACS Appl. Mater. Interfaces. 9 (37) (2017) 32054–32064, https://doi.org/10.1021/acsami.7b09652.
[55] Z. Yan, T. Pan, D. Wang, J. Li, L. Jin, L. Huang, J. Jiang, Z. Qi, H. Zhang, M. Gao, W. Yang, Y. Lin, Stretchable micromotion sensor with enhanced sensitivity using serpentine layout, ACS Appl. Mater. Interfaces. 11 (13) (2019) 12261–12271, https://doi.org/10.1021/acsami.8b22613.
[56] S. Pradhan, V.K. Yadavalli, Photolithographically printed flexible silk/PEDOT:PSS Temperature Sensors, ACS Appl. Electron. Mater. 3 (1) (2020) 21–29, https://doi.org/10.1021/acsaelm.0c01017.
[57] Y. Yang, Y. Song, X. Bo, J. Min, O.S. Pak, L. Zhu, M. Wang, J. Tu, A. Kogan, H. Zhang, T.K. Hsiai, Z. Li, W. Gao, A laser-engraved wearable sensor for sensitive detection of uric acid and tyrosine in sweat, Nat. Biotechnol. 38 (2) (2020) 217–224, https://doi.org/10.1038/s41587-019-0321-x.
[58] Y. Li, C. Zheng, S. Liu, L. Huang, T. Fang, J.X. Li, F. Xu, F. Li, Smart glove integrated with tunable mwnts/pdms fibers made of a one-step extrusion method for finger dexterity, gesture, and temperature recognition, ACS Appl. Mater. Interfaces. 12 (21) (2020) 23764–23773, https://doi.org/10.1021/acsami.0c08114.
[59] Y. Zhu, L. Lin, Y. Chen, Y. Song, W. Lu, Y. Guo, Extreme temperature-tolerant conductive gel with antibacterial activity for flexible dual-response sensors, ACS Appl. Mater. Interfaces. 12 (50) (2020) 56470–56479, https://doi.org/10.1021/acsami.0c17242.
[60] F. Zhang, H. Hu, M. Islam, S. Peng, S. Wu, S. Lim, Y. Zhou, C.-H. Wang, Multi-modal strain and temperature sensor by hybridizing reduced graphene oxide and PEDOT:PSS, Compos. Sci. Technol. 187 (2020), 107959, https://doi.org/10.1016/j.compscitech.2019.107959.
[61] Z. Wang, H. Zhou, W. Chen, Q. Li, B. Yan, X. Jin, A. Ma, H. Liu, W. Zhao, Dually synergetic network hydrogels with integrated mechanical stretchability, thermal responsiveness, and electrical conductivity for strain sensors and temperature alertors, ACS Appl. Mater. Interfaces. 10 (16) (2018) 14045–14054, https://doi.org/10.1021/acsami.8b02060.